Computational Materials Science 220 (2023) 112033

Contents lists available at ScienceDirect

Computational Materials Science

journal homepage: www.elsevier.com/locate/commatsci

Full length article

Electronic origin of Suzuki segregation of transition metal elements in face-centered cubic Co and Ni alloys

Dongsheng Wen *, Michael S. Titus

School of Materials Engineering, Purdue University, 701 West Stadium Ave, West Lafayette, IN 47907, USA

ARTICLE INFO

Keywords:
Suzuki segregation
Stacking faults
Ni-based alloys
Co-based alloys
Density functional theory

ABSTRACT

Solute segregation to stacking faults (also known as Suzuki segregation) has been employed to stabilize the planar defects to design desired plastic deformation mechanisms in Co- and Ni-based alloys. However, the solute segregation behaviors in intrinsic stacking faults (ISF) and the electronic origin of the segregation remain unclear in face-centered cubic Co- and Ni-alloys. In this study, we predicted the solute-ISF interaction energy for 3d, 4d, and 5d transition metal elements in FCC Co and Ni, using first-principles density functional theory calculations. The driving force of segregation can be attributed to the confluence of the local atomic distortions, charge density redistribution, electron orbital interactions, and local magnetic interactions between the solute and the solvent atoms. These driving forces and the relationships can be utilized in future alloy design efforts to improve mechanical properties via Suzuki segregation to planar defects.

1. Introduction

Advanced structural alloys exhibit excellent high-temperature mechanical properties stemming from the dislocations and stacking faults (SF) that interact with various obstacles. Studies have shown that solute segregation to the stacking faults, also known as Suzuki segregation [1,2], can (1) promote stable and effective planar barriers to dislocation motions and (2) induce local phase transformations to improve mechanical properties in superalloys, steels, and multi-principal element alloys [3–5]. The concept of utilizing Suzuki segregation to strengthen the materials motivates researchers to understand the phenomenon and implement it in integrated computational materials engineering (ICME) approaches [3,6–9].

In high-strength steels, the stacking fault energy (SFE) can be modified by control of Mn additions, which has been used to design desirable plastic deformation mechanisms to achieve good strength-ductility synergy [4]. The SFE of Fe-Mn-Al-Si steels decreases with decreasing Mn content so that SFs, martensitic transformations, and twinning can be activated as secondary deformation mechanisms [10,11]. As a result, extended dislocations in the matrix are less likely to cross-slip and are constantly blocked by the planar structures, leading to stronger strain hardening effects. In Co and CoNi-based superalloys, slight modifications in alloy compositions can lead to changes in which solute species will segregate to stacking faults and the resulting planar defect energies, significantly influencing high-temperature creep behavior [3,6,12,13]. Extensive works have been conducted to understand the Suzuki segregation in the planar defects of the γ'–Ni_3Al phase by high-resolution transmission electron microscopy and atom probe tomography [3,6,8,9,12,14–16]. First-principles and thermodynamic simulations have been used to study the driving force of segregation, in which new models have shown the ability to quantitatively predict the segregation concentration and energy at finite temperatures and compositions [7,9,17].

While most of the recent studies have focused on the superlattice planar defects in the γ' precipitates of superalloys, Suzuki segregation in the face-centered cubic (FCC) disordered phase remains unclear. The FCC phase plays an important role in Co- and Ni-based alloys. Superalloys contain about 30 to 40 vol.% of FCC phase, serving as the matrix phase strengthened by the cuboidal γ' precipitates [18]. Planar defects that shear the γ' phase originate from the dislocation/stacking fault interactions at the $\gamma - \gamma'$ interfaces [18]. For example, the MP159 superalloys (CoNiCr-based) maintain high strengths at elevated temperatures, thanks to the change from perfect dislocation glide to partial dislocation glide in the FCC phase [19]. The change of deformation mechanisms can be attributed to the solute segregations to the intrinsic stacking fault in the FCC phase by lowering the stacking fault energy, which could affect the nucleation of ϵ phase at high temperatures [19]. However, the origin of the segregation was not clearly studied [19]. Recent study by Feng et al. has also stated that "local phase transformation" in the γ' could be originated from the stacking fault interaction at the matrix-precipitate interface [20]. It is essential to understand how alloying elements can stablize the stacking faults to provide efficient

* Corresponding author.
E-mail address: wen94@purdue.edu (D. Wen).

https://doi.org/10.1016/j.commatsci.2023.112033
Received 2 June 2022; Received in revised form 9 January 2023; Accepted 13 January 2023
Available online 7 February 2023

barriers to increase high-temperature strengths. Therefore, a fundamental study of Suzuki segregation in the FCC phase is important to understand and control the dislocation interactions. Such studies can further improve the thermodynamic modeling of stacking faults, which has yet to be satisfied by the current thermodynamic database of the bulk phases.

For an FCC alloy, stacking faults comprise two or four layers of the hexagonal closed-packed planes (HCP). Because of this, the stacking fault energy can be modeled by considering two or four layers of HCP which comprise the stacking fault, bound by FCC/HCP interfaces [21]:

$$SFE = \Delta G^{fcc\rightarrow hcp} + 2\sigma^{fcc/hcp} \tag{1}$$

in which $\Delta G^{fcc\rightarrow hcp}$ is the phase transformation energy for the two layers of ISF, and $2\sigma^{fcc/hcp}$ represents the two interfaces between the FCC and the ISF. This approximation relies on accurate experimental measurements of the stacking fault widths, compositions, or accurate free energies to determine the interfacial term.

The equilibrium composition at stacking faults can be modeled by utilizing the segregation isotherm, developed by Ma et al. [22] and Feng et al. [9]. The interactions are composition- and temperature-dependent such that segregation follows the segregation isotherm [22]:

$$\frac{c_i}{1-c_i} = \frac{c_\infty}{1-c_\infty} exp\left(-\frac{\Delta E_i^{seg}}{kT}\right) \tag{2}$$

in which c_i is the solute concentration of plane-i adjacent to the stacking fault, c_∞ is the solute concentration far from the stacking fault, ΔE_i^{seg} is the segregation energy, k is Boltzmann constant and T is temperature. A negative value of the segregation energy indicates the driving force of segregation. Feng et al. considered the excess exchange potential and gradient contributions to ΔE_i^{seg} [9,22], given by:

$$\Delta E_i^{seg} = \Delta E_i^X + \Delta\mu_{c_i}^{ex} - \Delta\mu_{c_\infty}^{ex} - \kappa\frac{d^2c}{dx^2} \tag{3}$$

in which the ΔE_i^X is the solute-SF interaction energy, $\Delta\mu^{ex}$ is the excess exchange potential beyond the ideal mixing, and the last term is the energy related to the gradient of the segregation profile. When the solute concentration is dilute ($< 5at.\%$), the interaction energy likely dominates this expression, and thus can be used as surrogate to predict equilibrium concentration of solute at stacking faults. However, Feng et al. have shown that the excess potential and gradient contributions can be comparable to interaction energy in concentrated ranges [9]. Thus, in this work, we use the interaction energy as a surrogate for segregation energy.

Further applications rely on calculating the terms in Eq. (3) quantitatively. Rao et al. have calculated the interaction energies for Co, Cr, Nb, and Ta in the superlattice intrinsic stacking faults in γ' phase through first-principles calculations [7]. And Feng et al. demonstrated that the excess exchange potential could be modeled by the energies of ordered/disordered interactions using thermodynamic data [9,23]. This requires determining the solute interaction coefficients for the HCP and FCC phases beyond the ideal mixture, such as regular solution and subregular solution models [9]. The first-principles studies of the Suzuki segregation in FCC Co-Ni binary alloys have shown that the ISF cannot be treated by the bulk close-packed hexagonal phase (HCP), even though the ISF maintains the stacking sequence of the HCP phase across 2 to 4 layers (see Fig. 1(a)) [17]. In addition, the supercell method by including an ISF within the FCC matrix is useful to quantify the excess energy due to interfacial interactions [3,17,24]. The first-principles approach can be generally applied to concentrated systems and do not simply rely on the bulk phase energies to determine segregation.

To incorporate Suzuki segregation in alloy design within the ICME practices, current knowledge gaps should be addressed: (1) A systematic study has not been conducted across the important alloying elements in the periodic table for Co- and Ni-alloys to determine the solute interaction energies; (2) the electronic origin of the segregation behavior has not been fully understood. Therefore, this study employs first-principles supercell method to investigate the 3d, 4d and 5d elements in the intrinsic stacking fault of FCC Co and Ni alloys.

2. Methodology

2.1. Supercell methods for interaction energy calculations

Starting with the segregation energy Eq. (3), the interaction energy ΔE_i^X can be evaluated by the supercell method through first-principles simulations. The interaction energy is calculated by comparing the energy of the supercell with a solute atom in layer-i and the energy of the supercell with the solute in the FCC [7,9,17]:

$$\Delta E_i^X = E_i^X - E_\infty^X \tag{4}$$

in which ΔE_i^X is the interaction energy of solute-X in layer-i near the stacking fault, E_i^X is the total energy of the tilted supercell containing one X atom in layer-i, and E_∞^X is the total energy of the tilted supercell with one X atom far away from the stacking fault.

To quantify ΔE_i, we utilize a defected supercell containing an ISF by shifting the perfect FCC structure by a vector of $b = a/6[\bar{1}\bar{1}2]$ on the (111) plane, see Fig. 1(a) and (b). In this way, a tilted supercell along the [111] direction can be created from the FCC supercell with 3n number of (111) planes, as seen in Fig. 1(c) and (d). This study uses a 9-layered tilted supercell with four atoms per layer, see Fig. 1(d). The two innermost ISF planes are layer-1 and layer-9 when periodic boundary condition is applied. Previous studies have shown that nine atomic layers are sufficient to reduce the interactions between the ISF phase in two adjacent periodic images [17,24].

In the tilted supercell in Fig. 1(d), layer-1 is the ISF plane and layer-5 can be used to approximate E_∞^X. Negative interaction energy implies solute segregation to the stacking faults, and a positive value implies solute depletion from the stacking fault. DFT calculations are performed to calculate the interaction energies of 3d, 4d and 5d elements in the tilted supercells of Co and Ni. For simplicity throughout the paper, the term 'X-1' is used exclusively to represent the supercell with the solute-X atom in layer-1 (ISF plane). Similarly, 'X-5' is used exclusively for the supercell with the solute-X atom in layer-5 (FCC plane).

2.2. Density functional theory calculations

In this study, the tilted supercells contain nine (111) planes with four atoms per layer, as shown in Fig. 1(d). To quantify the energy dependence on cell sizes, larger supercells (81-atom) were constructed with nine atoms on the (111) plane. The ground state total energies of the supercells are calculated using the Vienna Ab-initio Simulation Package (VASP) [25,26]. The projector augmented-wave method [27] was used to model the ions and electrons interactions with a global cut-off energy of 450 eV. We used the Generalized Gradient Approximation (PBE-GGA) to approximate the exchange–correlation functionals [28]. Colinear spin polarization was considered for all supercells, and the initial magnetic moments for Co and Ni were set to 2 and 1 μ_B, respectively. We used a Γ-centered $16 \times 16 \times 4$ k-mesh for the 9-layered 36-atom supercell. The energy integration was done by the Methfessel–Paxton method [29] in the reciprocal space with 0.2 eV smearing for ionic relaxations. We used 10^{-4} eV and 10^{-5} eV energy differences for the convergence criteria of the ionic relaxation and the self-consistent loops, respectively. After ionic relaxations, a highly-accurate electronic calculation was carried out with the tetrahedron-Blochl method [30]. The tilted supercells of pure Co and Ni were fully relaxed before doping the solute atoms into the layers for ionic relaxation.

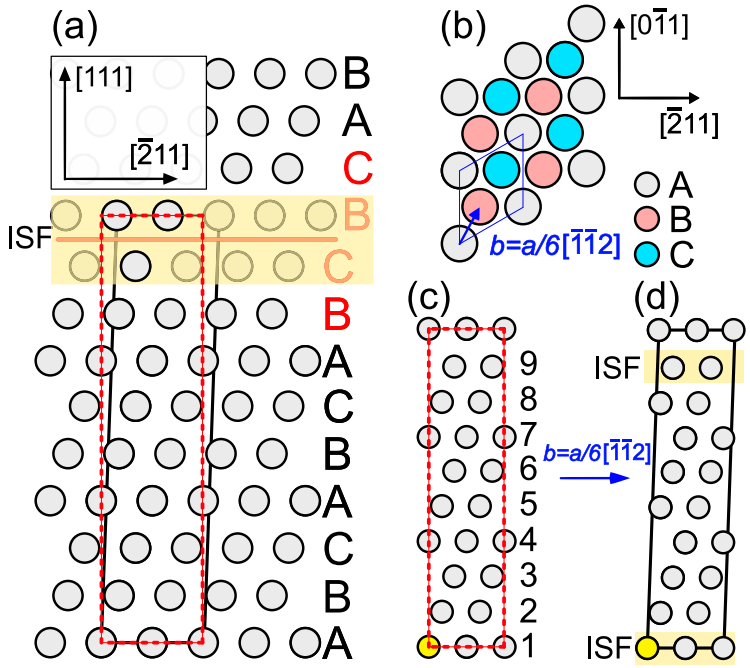

Fig. 1. Schematics of creating intrinsic stacking fault supercells. (a) Stacking sequence of the intrinsic stacking fault. (b) Displacement vector $b = a/6[\bar{1}\bar{1}2]$ for creating an intrinsic stacking fault on the (111) planes of the FCC structure. (c) The 9-layered supercell for FCC structure with a solute atom (yellow sphere) in layer-1. (d) The 9-layered tilted supercell with a solute atom (yellow sphere) in layer-1, layer-1 and layer-9 are ISF planes.
Source: Recreated from Ref. [17] with permission from Elsevier.

2.3. Charge density difference

Charge density analysis can be used to reveal the local bonding environments. The number of electrons is fixed for a system in which the charge density will redistribute when the solute shifts its position from an FCC plane to an ISF plane. This redistribution can be used to indicate bonding characteristics in the lattice. Therefore, the charge density difference (CDD) calculations were used to analyze the spatial redistributions of charge density around the solute placed in the ISF and the FCC planes. The charge density difference is defined by subtracting the atomic densities from the total density:

$$\Delta\rho = \rho_{A+X} - \rho_A - \rho_X \tag{5}$$

In our application, ρ_{A+X} is the charge density of the tilted supercell containing both the solvent-A and solute-X, ρ_X is the charge density of the tilted supercell with only the doped solute-X atom, and ρ_A is the charge density of the tilted supercell with only the solvent-A atoms. For example, the supercells for the ρ_{A+X}, ρ_A, and ρ_X are illustrated in Fig. 2(a). The net density difference over the whole supercell is zero because the total number of electrons in A+X is the same as the sum in A and X. However, the A-X bonding and the A-A bonding will be different, and the charge density will adapt to the new environment. The charge density calculations have been proved useful to various studies, including uncovering the deformation mode of materials under applied loads [31,32], determination of surface properties of adhesion [33], and the type of bondings of that leads to different ferroelectricity properties [34]. Therefore, to provide insights into the segregation, we focus on the difference in the charge densities for the solutes placed in the ISF and the FCC planes. The relative CDD shown in Fig. 2(b) is defined by $\Delta\rho' = \Delta\rho_1 - \Delta\rho_5$, in which $\Delta\rho_1$ and $\Delta\rho_5$ are the CDDs of X-1 and X-5 calculated by Eq. (5), respectively.

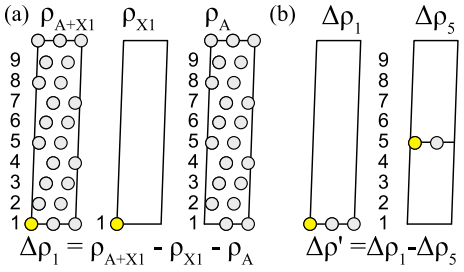

Fig. 2. (a) Schematics of the charge density difference calculation for solute-X (yellow atom) in layer-1 of the tilted supercell. (b) Schematics of the relative charge density difference calculation for solute-X in layer-1 and layer-5.

3. Results and discussions

3.1. Solute interaction energy in Co and Ni

The interaction energies of solutes in the innermost plane of the ISF are shown in Fig. 3 for Co and Ni systems. In Co, most of the elements from V-group to Co-group exhibit driving forces of segregation in the ISF (negative interaction energy), while Mn, Fe, W, and others show depletion (positive interaction energy). It has been shown that a segregation energy of about -20 meV can raise the Co concentration in the superlattice intrinsic stacking fault by about 25% [9]. The interaction energy ranges from −105 meV (Cr) to 151 meV (Mn), indicating that the SFE can be manipulated by controlling the alloying concentration.

In Ni, all the investigated elements show a driving force for segregation, ranging from −120 meV (Re) to −15 meV (Pt), as shown in Fig. 3(b). This implies that the solute elements may lower the stacking fault energy of pure Ni. According to experimental measurements, the probability of observing stacking faults increases with solute concentrations, ranking from Ti > Mo > W > V > Cr > Mn > Co > Cu > Fe [35,36]. This largely agrees with our interaction energy from low (segregating) to high (depleting): Mo < W < V < Ti < Cr < Co < Fe < Mn < Cu. The reasons for the discrepancies between the theoretical and experimental ranking can be manifold. The first and most important reason could be the accuracy of the experiments that measured the stacking fault density [35]. The uncertainty of the stacking fault density measured by the X-ray diffraction technique can be up to 0.002, which

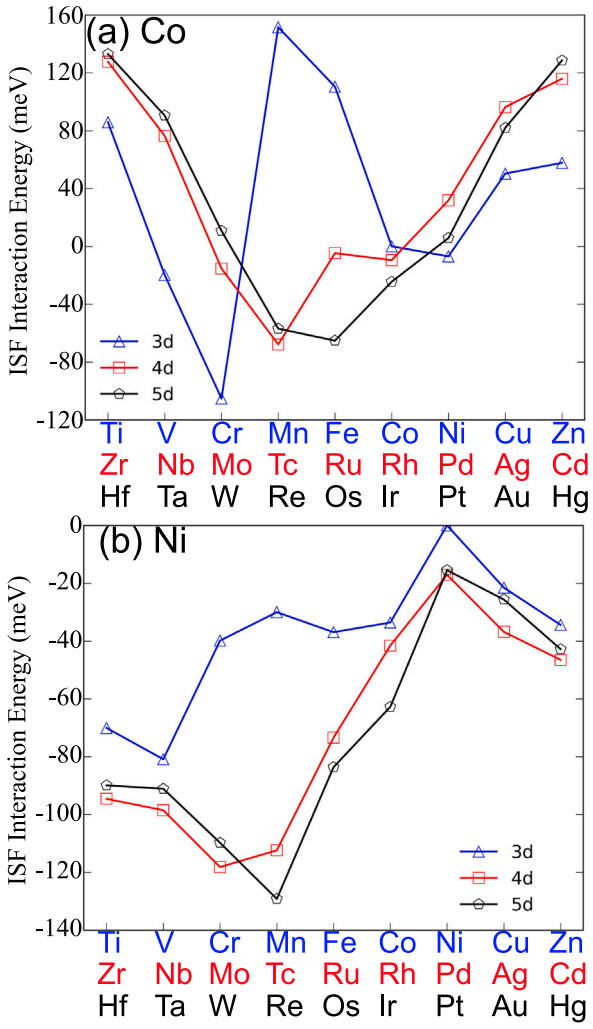

Fig. 3. Solute interaction energies in the ISF for 3d, 4d and 5d elements. (a) Co alloys. (b) Ni alloys.

is significant for the absolute densities of about 0.005 to 0.01 for Ni-based alloys [35]. Second, the stacking fault segregation and energy are compositionally dependent. The ranking determined from the experiments (SF density: 0.01–0.03) is actually from concentrated solutions higher than 10 at.%, in which configurational entropy can play an important role. Third, the heat treatment history can also influence the SF density; however, the recrystallization temperature and time were unclear for the alloys. All the above reasons can lead to discrepancies in the theoretical and experimental measurements. The 4d and 5d elements exhibit similar trends of interaction energy: from left to right, the energy decreases to group-7 elements and then increases. However, 3d elements, especially Cr, Mn, and Fe, show different behaviors. This can be partly attributed to the magnetism of Cr, Mn, and Fe. Niu et al. have shown that in CrMnFeCoNi and CrCoNi alloys, Cr, Mn, and Fe atoms have higher magnetic moments than Ni, and their magnetic moments can change significantly within the FCC/HCP supercells [5].

3.2. Local atomic distortion

Solutes with different atomic radii create local lattice distortions in the supercell. The local atomic distortion (LAD) is quantified by the net displacement of an atom from the input structure [37]:

$$\mathrm{LAD} = \|p - p_0\| \tag{6}$$

in which $p_0 = (x_0, y_0, z_0)$ and $p = (x, y, z)$ are absolute coordinates of an atom before and after ionic relaxation, respectively. This definition may not be able to exclude cooperative displacements of all atoms after ionic relaxation, which results in non-zero LAD even when the true distortion is negligible. To avoid the cooperative displacements, we introduce an correction term for each atomic plane-i:

$$\mathrm{LAD} = \|p - p_0 - d_i\| \tag{7}$$

where d_i is the cooperative displacement vector defined by $d_i = c_i - c_{i,0}$, in which $c_{i,0} = \frac{\sum_j^n p_{j,0}}{n}$ and $c_i = \frac{\sum_j^n p_j}{n}$ are the averaged position of the four atoms before and after relaxation on plane-i, respectively, and n represents the number of atoms on plane-i.

In this way, the cooperative displacements on plane-i can be avoided and the local displacements in the plane can be properly captured. The means and standard deviations of the LAD for the four atoms in each (111) plane can quantify the planar atomic distortions from layer-1 to layer-9, which are shown in Fig. 4. To compare the lattice distortion (TAD) in the whole supercell, TAD can be calculated by summing the LAD for all the atoms in the supercell, as shown in Fig. 5.

The planar LADs for 'X-1' and 'X-5' structures show that distortion is stronger in the planes adjacent to the doped-plane, see Fig. 4(a) for Co and Fig. 4(b) for Ni. For the X-1 structure, layer-2 and layer-9 show substantial distortions while the doped layer-1 is distorted mildly, and the distortion decays to negligible with increasing distances from the doped plane. Similar behaviors can be seen in the X-5 structure, in which the doped layer-5 presents negligible distortion. From top

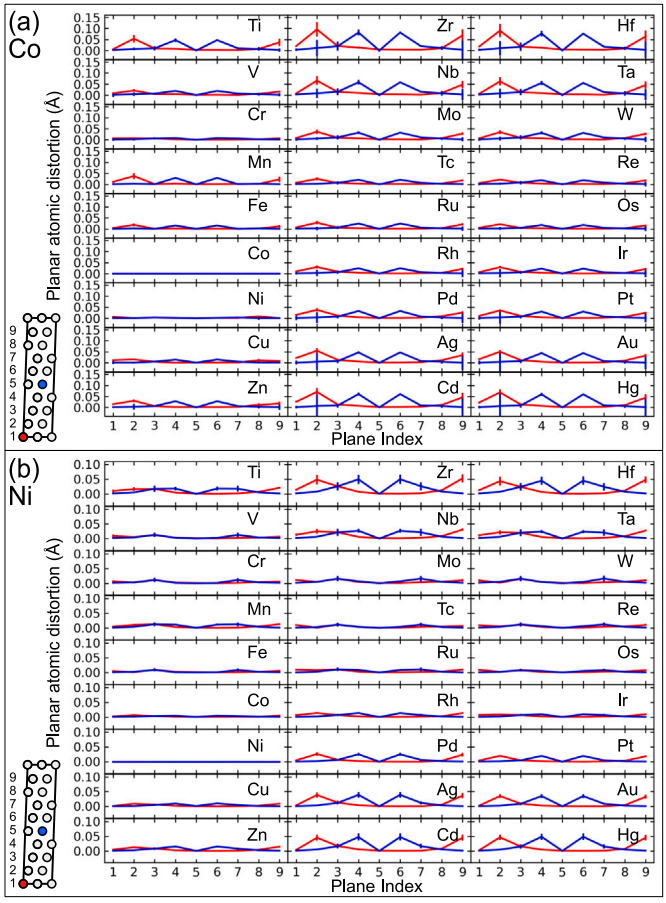

Fig. 4. Planar atomic distortion for every (111) plane in the (a) Co tilted supercell and (b) Ni tilted supercell. The red lines are for the solutes in the ISF plane (plane-1). The blue lines are for the solutes in the FCC plane (plane-5). The values are the average of the LAD of each atom in the plane. Error bars represent standard deviation in individual LAD for the atoms in each plane.

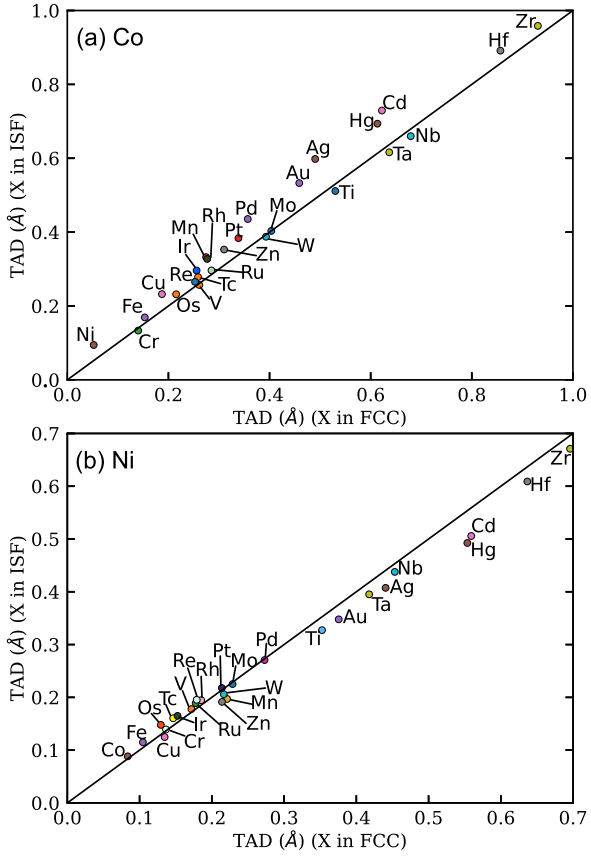

Fig. 5. Total atomic distortion of the supercell with a solute in the ISF (plane-1) vs. total atomic distortion of the supercell with the solute in the FCC (plane-5). For Co-alloys (a) and Ni-alloys (b), solutes produce similar total distortions when placed in ISF and FCC planes.

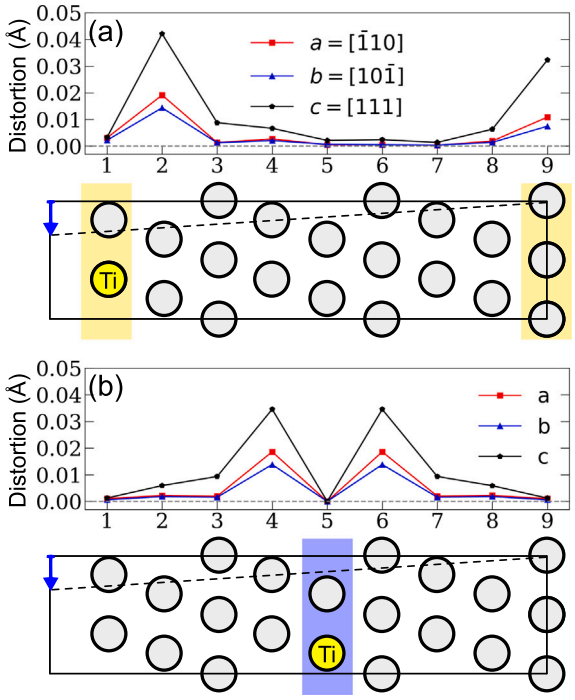

Fig. 6. Ti in Co supercells: Local distortions in three directions of the tilted supercell. *a* and *b* are for the (111) in-plane distortion, and *c* is for the (111) out-of-plane distortion. (a) is for the Ti atom placed in layer-1 of the Co supercell. The yellow-highlighted planes represent the ISF planes. (b) is for the Ti atom placed in layer-5 of the Co supercell. The blue-highlighted plane represents the FCC plane with the solute atom.

to bottom, the middle 4d and 5d elements show relatively smaller distortions, and the distortions gradually increase from the middle to group 4 and to group 12 elements. Co creates negligible distortions in the Ni supercell, and vice versa, mainly due to the similarities in atomic radii, lattice structure, and electronic configurations between the two elements.

For solutes in the Co supercell, the contributions of the in-plane and out-of-plane distortions are shown in Fig. 6 where local distortions of the planes are decomposed into three different vectors of the supercell. For example, when the Ti atom is placed in layer-1, the magnitudes of the in-plane (*a* and *b*) and out-of-plane (*c*) distortions are comparable for each plane, see Fig. 6(a). The largest distortions are within layer-2, followed by layer-9. In contrast, when the Ti atom is placed in layer-5, layer-4 and layer-6 exhibit the largest distortions, see Fig. 6(b). The curves in Fig. 6(b) exhibit a symmetrical manner on both sides of layer-5. This can be attributed to the geometry of the tilted supercell that layer-5 is the middle plane of the cell. Similarly, the discrepancy between the distortions of layer-9 and layer-2 can be attributed to the fact that layer-9 is one of the ISF planes while layer-2 is outside the ISF.

For solutes in the Ni supercell, the trends of local distortions are similar to the Co supercell mentioned above, see Fig. 7. Compared with the Co supercell, the magnitudes of distortions in the Ni supercell are lower. Another difference in the distortions between the Ni-Ti supercell and the Co-Ti supercell is that, for Ti-1 in the Ni supercell, the 2NN planes also exhibit distortions along the *c*-direction, see Fig. 7(a). This out-of-plane interaction might be because the ISF is more stable in Co with a stacking fault energy of about −110 mJ/m^2, while the SFE of

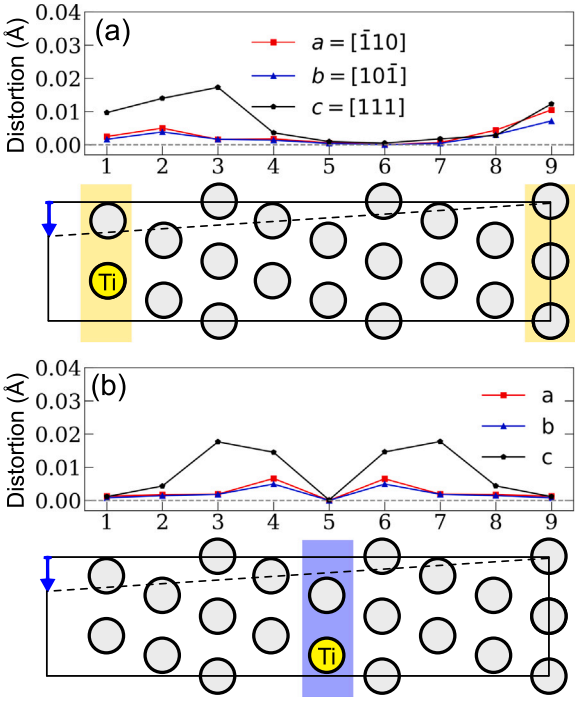

Fig. 7. Ti in Ni supercells: Local distortions in three directions of the tilted supercell. *a* and *b* are for the (111) in-plane distortion, and *c* is for the (111) out-of-plane distortion. (a) is for the Ti atom placed in layer-1 of the Ni supercell. The yellow-highlighted planes represent the ISF planes. (b) is for the Ti atom placed in layer-5 of the Ni supercell. The blue-highlighted plane represents the FCC plane with the solute atom.

Ni is about 125 mJ/m^2 [17]. For other solutes in both systems, similar observations can be made. With such observations, it can be confirmed that solute atoms generate local distortions, which will fade away with increasing atomic distances. Therefore, the interaction energy can be partially related to the differences between the distortions in the 1NN bonds formed in the ISF and FCC layers.

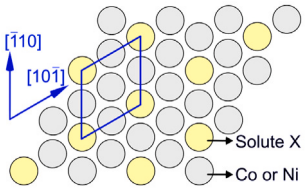

Fig. 8. The ordered structure of Co_3X or Ni_3X for a four-atom (111) plane containing one solute atom (yellow) and three solvent atoms (gray).

It is important to note that the solute-doped planes exhibit lower distortions, see layer-1 in Fig. 6(a) and layer-5 in Fig. 6(b). This is because each (111) plane contains four atoms that, when replacing a Co atom with the solute atom, an ordered structure will be formed within the plane with a composition of Co_3X, see Fig. 8. This ordered structure reduces the in-plane distortion of the solute plane while causing distortions in the adjacent planes. For the larger 81-atom supercells without the in-plane ordered structure, the in-plane distortions are higher for the solute-plane (See the example in Figure S2 in the supplementary document). In addition, it is also noted that the Ti-1 plane shows larger distortions than the Ti-5 plane even though they maintain the same ordered structure. It is more likely that the ISF structure causes the distortions.

Fig. 5 shows that the total distortions are comparable for X-ISF and X-FCC supercells. The relationship between the interaction energy and the total lattice distortion is weak (not shown here, see Figure S3 in the supplementary document). Therefore, it is reasonable that the solute interacting with the adjacent atoms locally by affecting the bond lengths between the solute and solvents. To link the interaction energy with the local bond lengths, the averaged bond length can be defined by the mean of the first nearest-neighbor bonds between the solute and solvent atoms:

$$R[X] = \frac{\sum_j^{12} \|p_j - p_s\|}{12} \tag{8}$$

in which p_j represents the positions of the 1NN solvent atoms around the solute atom with the position of p_s. The coordination number is 12 for solutes in both the ISF and FCC planes. Using Eq. (8), the averaged bond lengths of X-ISF (R[X-ISF]) and those of X-FCC (R[X-FCC]) are calculated.

The correlation between the interaction energy and the differences of the bond lengths for X-ISF and X-FCC solutes are shown in Fig. 9. For

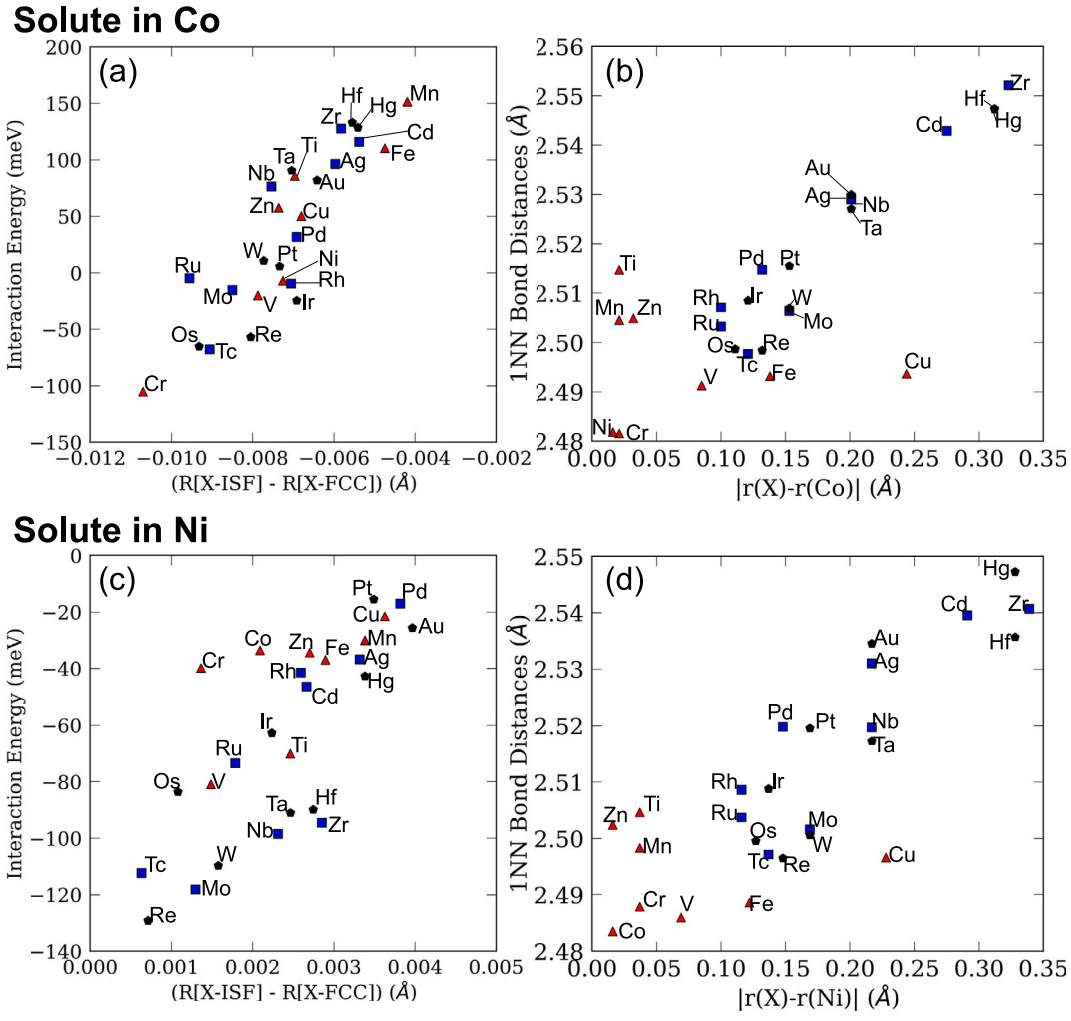

Fig. 9. Relationship between the interaction energy and the 1NN bond length difference with solutes in the ISF and the FCC layers. For Co supercells: (a) Interaction energy vs. the difference between the 1NN bond lengths of the X-ISF (layer-1) and the X-FCC (layer-5); (b) the 1NN bond lengths of X-ISF increases with the radius mismatch between the solute atom and the Co atom, except for 3d elements. For Ni supercells: (c) Interaction energy vs. the difference between the 1NN bond lengths of the X-ISF (layer-1) and the X-FCC (layer-5); (d) the 1NN bond lengths of X-ISF increases with the radius mismatch between the solute atom and the Ni atom, except for 3d elements.

both Co and Ni supercells, the interaction energy generally increases when the difference between the bond lengths of the X-ISF and X-FCC supercells increases (see Fig. 9(a) and (c)). As also pointed out by Feng et al. in the study of solute-defect interaction in the Ni-based superalloys, the magnitude of the interaction is generally related to the distortion, and the change of positions around the dislocation core and grain boundary [9]. The distortion can first be related to the atomic misfit between the solute and solvent atoms. The 1NN bond lengths of X-ISF generally increase with increasing atomic radius misfits (r(X)-r(Co or Ni)) calculated by the Wigner–Seitz radius (r(X), r(Co) and r(Ni)) of the PBE pseudopotentials [28], especially for 4d and 5d elements, as shown Fig. 9(b) and (d). For 3d elements with similar atomic misfits, the correlation between the 1NN bond lengths and the atomic misfit is weaker. For these 3d elements, the planar distortions are generally smaller than those by the 4d and 5d elements, see Fig. 4. The valence electronic configurations of 3d elements are 4s3d, sharing similarities with Co ($4s^2 3d^7$) and Ni ($4s^2 3d^8$). This indicates that other interactions may be involved, such as electronic and magnetic interactions, which will be discussed later.

3.3. Charge density difference

Charge density difference reflects the formation of bonding, which can be visualized by the spatial mapping of charge density redistribution around the solute atoms. The redistributions mainly occur between the 1NN atoms and the solute, and the CDD in other regions is negligible. The strength of the bonding can be qualitatively interpreted from the morphology of the contours of the CDD between the solute and solvent. For example, Fig. 10(a) shows the CDD around the Cr and 1NN Co atoms in the ISF plane. The cyan isosurface around the Cr atom in the middle shows a depletion zone of charge density, and the yellow isosurfaces show an accumulation zone of charge density. It can be seen that the accumulation zone is in between the Cr-Co bonds, indicating that Cr is contributing the charge density to the bonding region, see Fig. 10(a) and (b). The morphology of the isosurfaces in the ISF and the FCC planes are different regarding the different stacking below the middle plane. For the Cr in the ISF plane (Fig. 10(a)), the upper and lower planes have the same stacking structure, leading to symmetrical patterns of isosurfaces. For the Cr in the FCC plane (Fig. 10(b)), the lower plane is C-stacking, and the accumulation zone is adapted to the Cr-Co bonds.

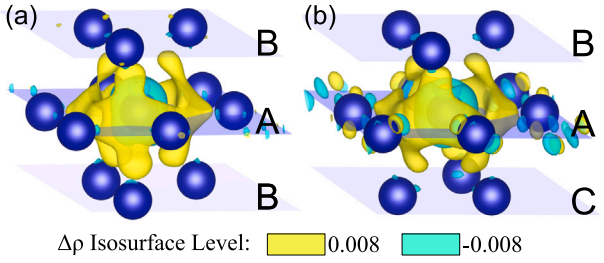

Fig. 10. Charge density difference isosurface around the Cr and the 1NN Co atoms in (a) the ISF and (b) the FCC planes. The blue spheres are 1NN Co atoms and the Cr atom is in the middle of the A plane. The yellow and cyan regions represent the positive and negative values of CDD, respectively.

The shapes and magnitudes of the accumulation zones around the solutes are related to the strengths of the bondings. For the in-plane distribution, the hexagonal accumulation zones on the ISF/FCC plane show that charge redistributes around the solute and adjacent solvent atoms, while the intensity can be slightly different (see the middle planes in Fig. 11(a) and Fig. 11(b)). The in-plane CDDs of Cr-1 in Fig. 11(a) show solutes' abilities to contribute charge densities to the bondings between the Cr and Co atoms. The planar CDDs for other solutes are shown in Figure S6 in the supplementary document. In

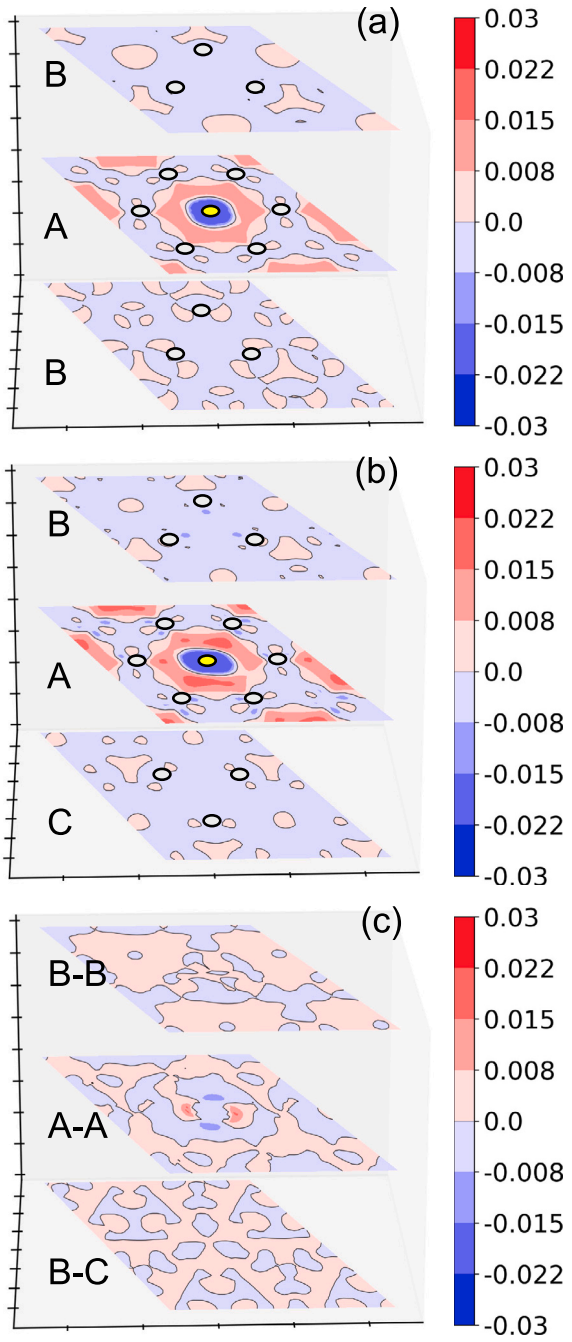

Fig. 11. (a) For the Cr-1 in the Co supercell, CDD contour plots of the layer-9 (bottom), layer-1 (middle) and layer-2 (top). (b) For the Cr-5 Co supercell, CDD contour plots of the layer-4 (bottom), layer-5 (middle) and layer-6. (c) Relative CDD between the layers in (a) and (b): Bottom: comparison between layer-9 of Cr-1 and layer-4 of Cr-5; Middle: comparison between layer-1 of Cr-1 and layer-5 of Cr-5; and Top: comparison between layer-2 of Cr-1 and layer-6 of Cr-5. Yellow and gray spheres represents the Cr and Co atoms.

general, the accumulation zones slightly shrink from the left to right side of the periodic table, indicating that the solute–solvent interactions are weakened. For the out-of-plane distribution, layer-9 and layer-2 near the solute-doped layer-1 exhibit slightly different CDD even though they have the same atomic stacking (see the bottom and top layers of Fig. 11(a)). The CDDs of layer-3 and layer-5 are rotated 60° about the center (see the bottom and top layers of Fig. 11(b)). However, the CDD intensities of the upper and lower planes drop below 1/5 to

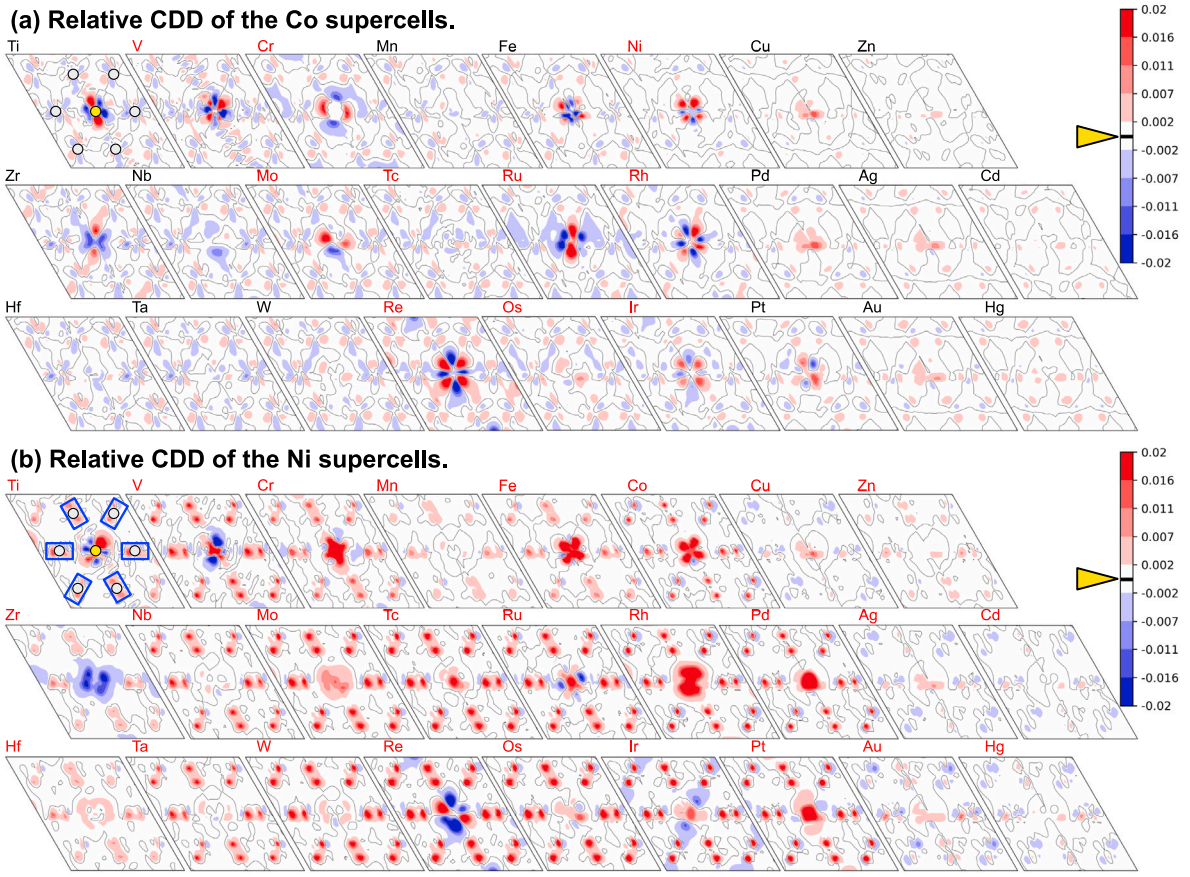

Fig. 12. (a) Co-alloys and (b) Ni-alloys: Relative CDD contour plots of the X-1 planes with the solute atom in the middle, the yellow sphere denotes the solute and gray spheres denote the solvent atoms in the first plot. The red and blue regions represent positive and negative values of relative CDD, respectively. The black lines represent the zero contour marked on the scale bar. The elemental labels in red color represent the negative interaction energies.

1/10 of the intensity of the solute plane, see the top and bottom layers in Fig. 11(a) and Fig. 11(b).

The relative CDD is introduced by comparing the CDDs around X-1 and X-5, as shown in Fig. 11(c) for Cr in the Co supercell. Although the in-plane structures of the ISF and FCC planes are similar, charge is redistributed differently around Cr-1 and Cr-5, which can be linked to the segregation behaviors of solute and solvent atoms. The peaks and valleys on the relative CDD plot indicate preferential bonding directions. As shown in Fig. 4, Fig. 7, and Fig. 6, the in-plane distortion is lower than 0.001 Å on the solute planes; therefore, the differences of redistribution are less likely to be related to the in-plane relaxation. The relative CDD mappings for all the solutes are shown in Fig. 12 for Co and Ni supercells. The charge density redistributes with distinct stronger peaks and deeper valleys around the solute atoms, especially for Ti, V, Cr, Fe, Ni, Zr, Mo, Ru, Rh, Re, Ir, and Pt. Their relative CDDs exhibit redistribution mainly around the solute center in different directions not necessarily aligned with the solute-solvent bondings. For these elements in Co (Fig. 12(a)), although most of them tend to segregate to the stacking fault, including V, Cr, Ni, Mo, Ru, Rh, Re, and Ir, the morphology is complicated that one cannot rely on a simple pattern to indicate negative segregation. For the Cu- and Zn-groups, the relative CDD intensities are weaker, which is due to the facts that their CDDs are comparable and weaker around X-1 and X-5. When solutes are placed in the Ni supercells, the charge redistributions intensify not only around the solute atom but also around the 1NN Ni atoms, see Fig. 12(b). For example, the relative CDD shows two distinct peaks around the Ni atoms in the Ni-Ti plot 12(b). Because the accumulation regions strongly correlate to the 1NN bonding directions, it can be confirmed that the Ni-X bondings within the ISF plane are enhanced. This can also explain that all the solutes in the Ni system exhibit segregation tendency while only some of them show segregation to the Co ISF.

3.4. Density of states

The bonding environment can be revealed by the site projected density of states (DOS) of solutes and the 1NN solvent atoms. For solute elements from left to right in the periodic table, the projected d-orbital DOSs of the elements exhibit shifting of the high energy states of the majority spin from above the Fermi level to lower energy states, see Figure S4 in the supplementary. This change of DOS is also observed for the investigated elements in their pure states [38]. This results in different solute–solvent interactions through the d-d interactions. For example, the role of d-d hybridization between the Ti-1 and 1NN Co leads to the coexisting peaks of PDOS at around 1.5 eV above the Fermi level, as indicated by the shaded box in Fig. 13(a). For the Co atom in layer-5 (far away from the Ti-1) in the same supercell, no d-d interaction can be detected. Similarly, for the Co atoms in layer-2, layer-3, and layer-4, only weak interaction was observed for layer-2, and no interaction can be detected for layer-3 and layer-4 atoms, see Figure S3 in the supplementary document. This can further confirm that d-d interactions can be formed between 1NN neighbors but are not likely to influence atoms with longer distances. When Ti is in the FCC plane, the 1NN Co atoms also show d-d hybridization (see Fig. 13(b)). With similar observations across all the investigated elements in both Co and Ni supercells, it can be concluded that the d-d interaction between the solute and solvent atoms cuts off within the 1NN.

The d-d hybridization influences the solute interactions in the ISF and FCC structures, which may be reflected around the Fermi level in

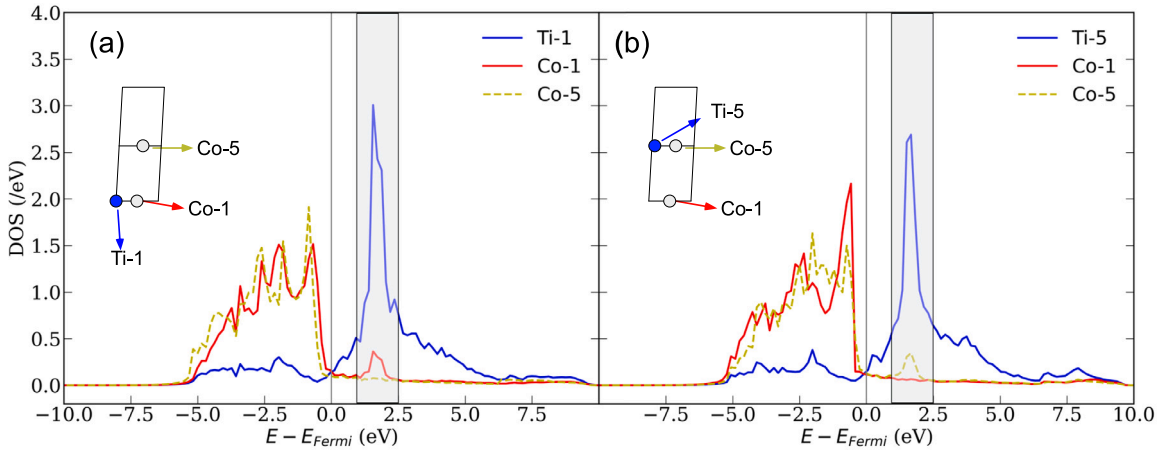

Fig. 13. (a) Partial density of states of d-orbitals of selected sites in the Ti-1 supercell: Ti-1 is for the Ti site, Co-1 is for the 1NN Co in layer-1, and Co-5 is for the Co atom in layer-5. (b) Partial density of states of d-orbitals of selected sites in the Ti-FCC supercell: Ti-5 is for Ti in layer-5, Co-5 is for the 1NN Co in layer-5, and Co-1 is for the Co in layer-1. The 1NN Co and Ti present coexisting peaks at around 1.5 eV above the Fermi level. The Co atoms far away from the Ti presents no peaks at the same energy level.

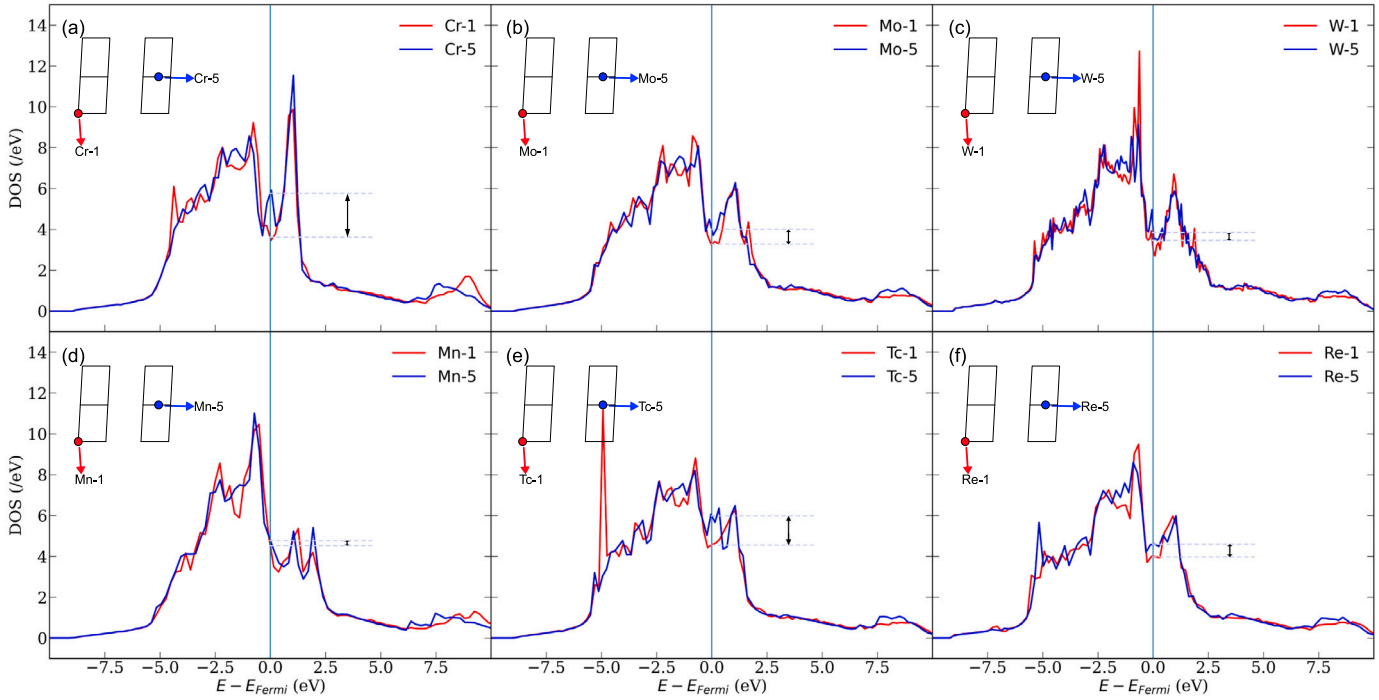

Fig. 14. Projected DOS of the solutes (a) Cr, (b) Mo, (c) W, (d) Mn, (e) Tc, and (f) Re in layer-1 and layer-5 of the Co supercells. The deeper gap of Cr-1 than Cr-5 indicates that Cr is more stable in the ISF than in the FCC plane of the supercell, corresponding to a negative interaction energy. For Mo and W, the gaps are closer and can be related to the higher interaction energies of these two elements. For Mn, Tc, and Re, same trend can be observed.

the DOS. It has been shown that the stability of a structure may be evaluated by the pseudo-gap at the Fermi level [39–41]. A lower DOS (or a deeper pseudo-gap) at the Fermi level may indicate a more stable structure, which means a larger distance between the pseudo-gaps of the X-ISF and X-FCC indicates negative interaction energy. For Cr, Mo, and W in the same group, the projected DOSs at the Fermi level of the solute in layer-1 (ISF) is lower than those when the solute is in layer-5 (FCC) (see Fig. 14(a)), implying that these elements favor the ISF structure with a covalent-like environment [39]. In addition, at the Fermi level, the difference between the pseudo-gaps of Cr-1 and Cr-5 is larger than that for Mo and W, which can be linked to the lower interaction energy of Cr than Mo and W in the ISF. For the Mn-Tc-Re group, the same trend can be observed: Mn has the highest interaction energy with the narrowest pseudo-gap difference, followed by Re and Tc. It is also noticed that the sign of the pseudo-gap difference may not be directly reflected in the sign of the interaction energy. For Mn with the highest positive interaction energy, the pseudo-gap of the Mn-ISF is still slightly lower than that of the Mn-FCC. We observe similar behaviors in the V-Ta-Nb and Fe-Ru-Os groups in the Co supercell.

To further relate the interaction energy to the pseudo-gap difference, a direct and linear correlation can be observed for 3d elements in the Co supercells, see Fig. 15(a). A more negative pseudo-gap difference indicates that the solute is energetically-favorable in the ISF plane over the FCC plane. As discussed previously, the interaction energies for 3d metals are less likely to be contributed by atomic misfits due to lower lattice misfit, as shown in Fig. 9. Therefore, the pseudo-gap plays an important role in comparing the solute-ISF and solute-FCC interactions for the 3d metals. For 4d and 5d elements, the correlation is not strong (Fig. 15(b), (c), (e), and (f)), which can be due to the stronger lattice misfit interactions, shown in Fig. 9. For 3d elements in Ni, the linear

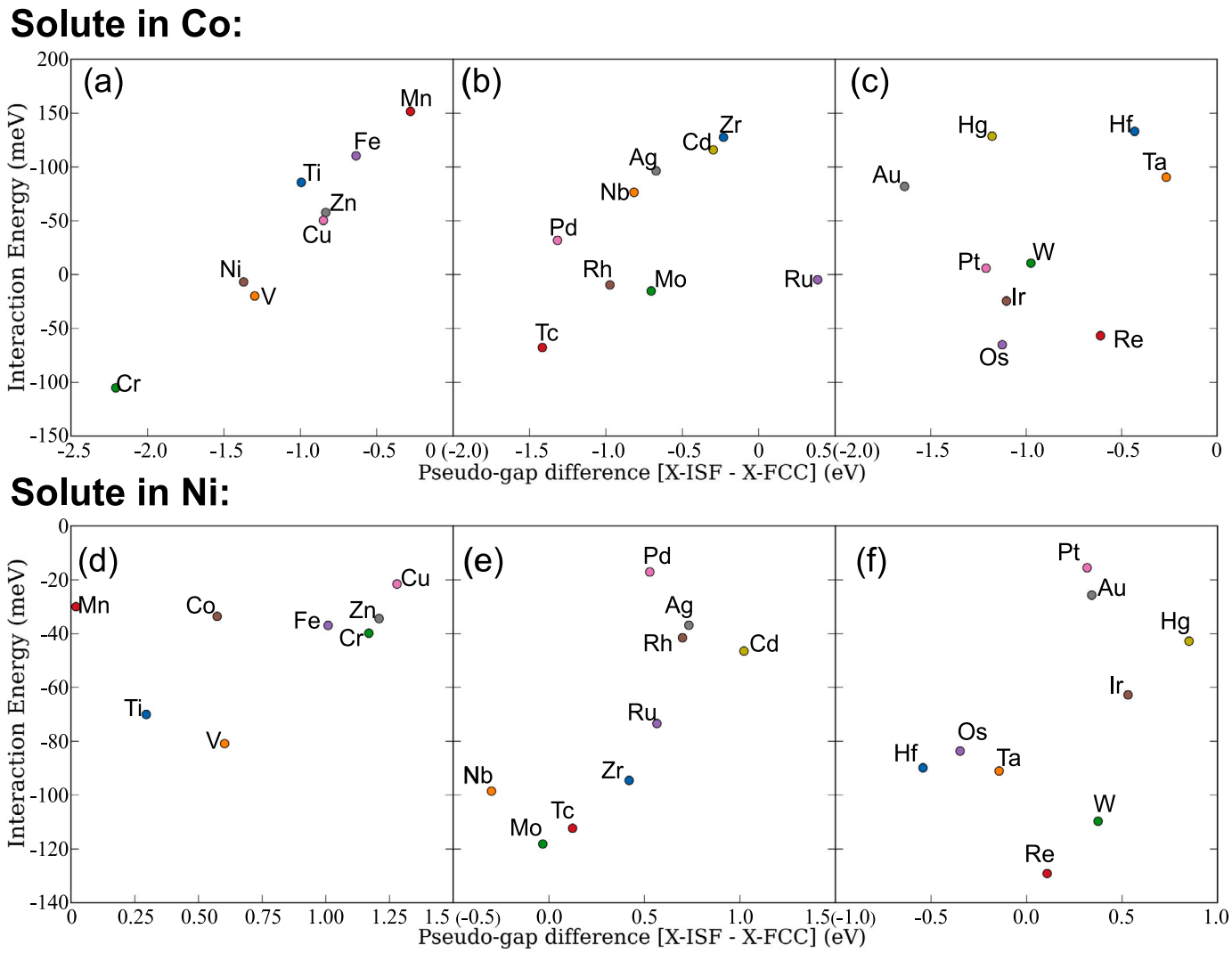

Fig. 15. Interaction energy vs. the pseudo-gap difference between the X-ISF and X-FCC partial DOS. (a)–(c) are for 3d, 4d, and 5d elements in Co supercells. (d)–(f) are for Ni supercells.

relationship may be maintained for V, Cr, Fe, Cu, and Zn, while Ti, Mn, and Co remain unclear. This may be related to the findings that 3d elements exhibit more subtle d-d interactions with Ni [39].

3.5. Magnetization

The d-d hybridization changes the local magnetizations in the supercell within the 1NN bonds. As shown in Fig. 16, the differences between the total magnetic moments of the X-1 and X-5 supercells are less than one μ_B. For 3d elements in Co, no direct relationship can be drawn between the interaction energy and the magnetization difference between the X-1 and X-5 supercells (Fig. 16(a)). For 4d and 5d elements in Co and Ni, we found that the interaction energy generally becomes more negative when the magnetic difference decreases between the X-1 and X-5 supercells, as seen in Fig. 16(b)–(c) and Fig. 16(e)–(f). The electronic magnetization originates from the difference between the majority and minority spins up to the Fermi level, indicating that d-d hybridization influences the majority spin more than the minority spin. For 3d elements in the Ni supercell, a relationship may be observed that lower magnetization in the X-ISF cell leads to lower interaction energy (except for Cr), see Fig. 16(d). This can be related to the local magnetization around the solute plane for the Cr-containing Ni supercells, which will be discussed later.

In order to show how the solute atoms enhance/frustrate the local magnetic moments, Fig. 17 plots the planar magnetizations across the (111) layers in the supercell. The local magnetic fluctuation vanishes with increasing distances from the solute plane, see Fig. 17(a). The same trends can be seen for solutes in the FCC plane of the supercell. We notice that for Cr-, Tc-, and Os-added supercells, the magnetizations of the 1NN planes to the solute plane are slightly affected, see Fig. 17(a), (c), and (e). A closer inspection of the planar magnetization reveals the lengths of magnetic interactions in the supercell. For example, when doping Cr in the plane, the magnetizations of the upper and lower planes to the solute plane are not at the solvent level, see Fig. 17(a); similar observations can be made for Tc (Fig. 17(b)) and Os (Fig. 17(c)) for the Co system or Fig. 17(g), (i) and (k) for the Ni system. However, for elements such as Mn, Ru, and Ir, the magnetic frustration/enhancement is confined only to the solute plane and the rest of the atomic planes maintain the same level of pure Co or Ni (see Fig. 17(b), (d) and (f) for Co or Fig. 17(h), (j) and (l) for Ni). In the periodic table of the transition metals, longer-range magnetic interactions are observed for elements on the left side, such as Ti-, V-, and Cr-group. For groups after the Fe-group, the magnetic interactions are only within the solute-plane. This may partially explain the energy-magnetization trends in Fig. 16 that Ti, V, Zr, Nb, Mo, Ru, Tc, Hf, Ta, W, Re, and Os exhibit relatively lower interaction energies. As seen in Fig. 17(g), Cr enhances the local magnetic moment on the

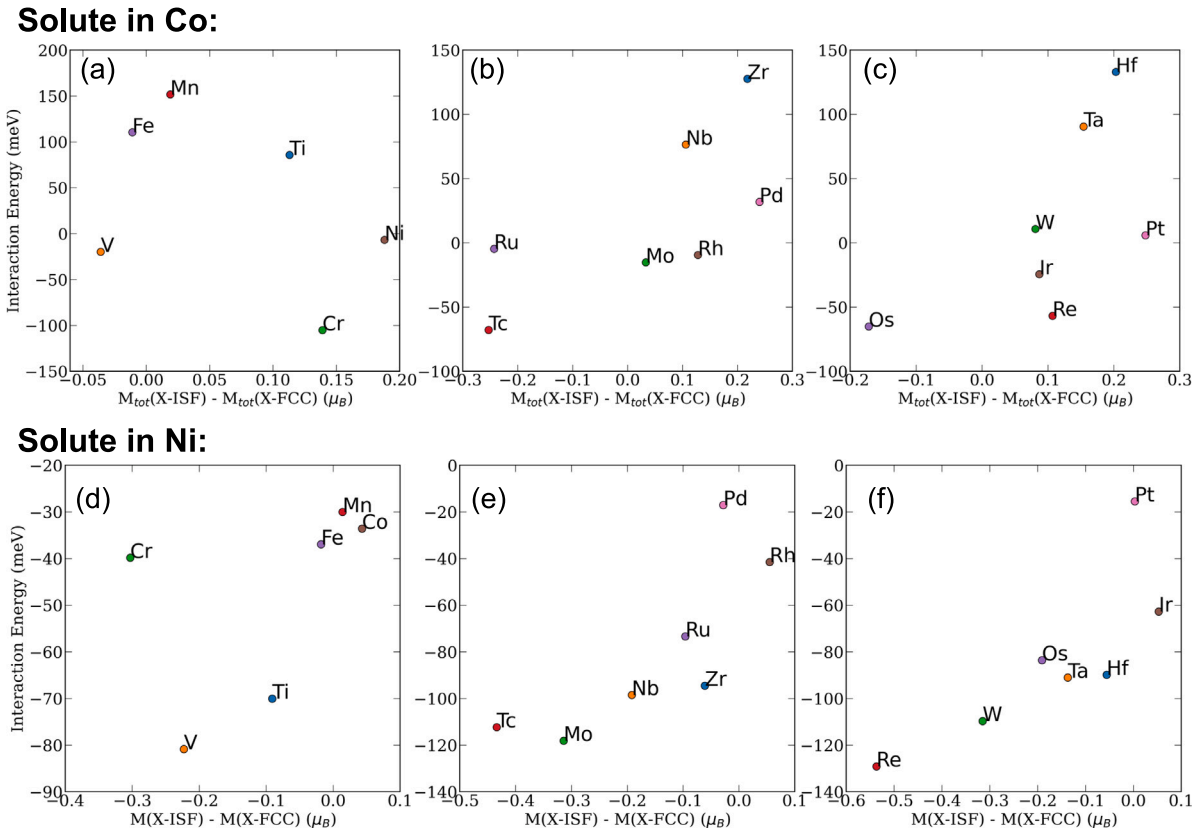

Fig. 16. Interaction energy vs. the difference between the magnetic moments of the supercells with solutes in the ISF (layer-1) and the FCC plane (layer-5). (a)–(c) are for Co-alloys and (d)–(f) are for Ni-alloys.

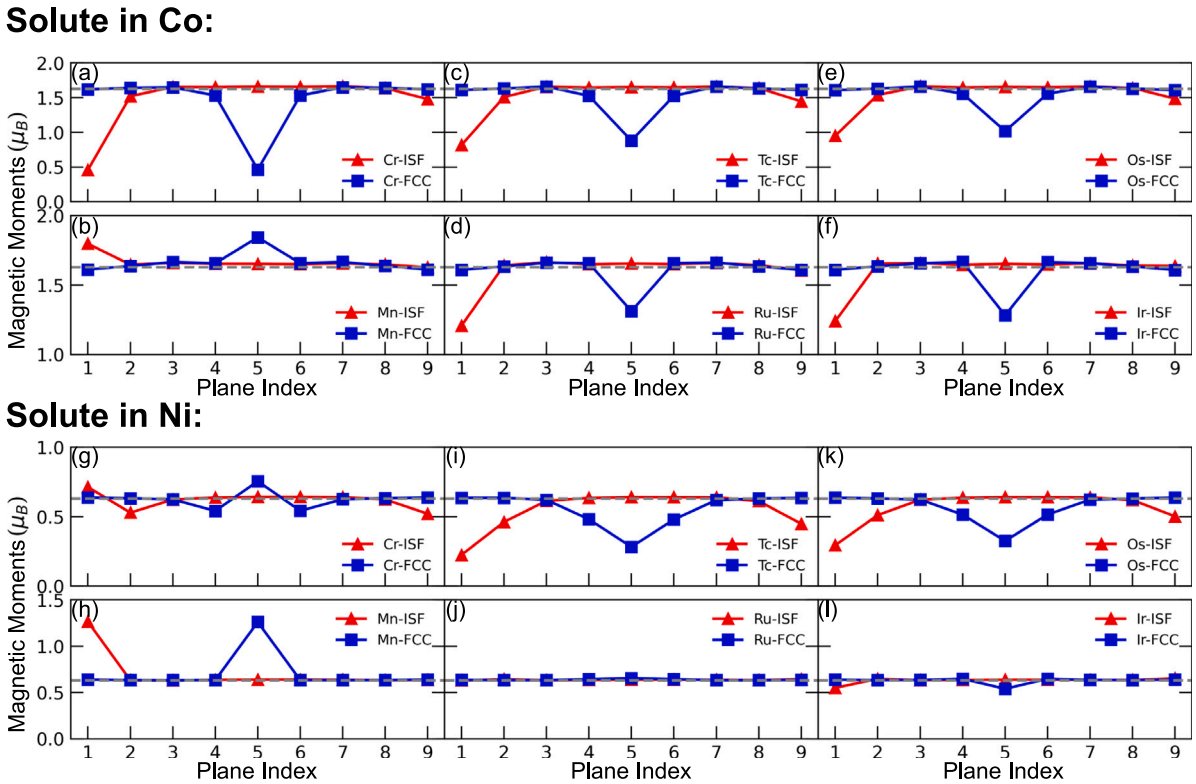

Fig. 17. Planar magnetic moments (normalized to per atom) of the tilted supercells with solute-X in layer-1 and layer-5. (a)–(f) are for Co supercells: (a) Cr, (b) Mn, (c) Tc, (d) Ru, (e) Os and (f) Ir. (g)–(l) are for Co supercells: (g) Cr, (h) Mn, (i) Tc, (j) Ru, (k) Os and (l) Ir. Red lines are for solutes in layer-1, blue lines are for solutes in layer-5, and the dashed gray lines are for magnetizations of pure Co or pure Ni.

solute plane but frustrates the moments on the adjacent planes with a comparable magnitude, which is unique among all the elements investigated. In fact, Cr and Mn are well-known to disturb the local magnetic moments and exhibit different magnetic states in the Cantor alloy [5]. Such interaction may be the reason for the breakaway from the energy-magnetization relationship observed in Fig. 16(d).

4. Conclusions

We studied the Suzuki segregation of the 3d, 4d, and 5d transition metals in the intrinsic stacking fault of the FCC Co and Ni alloys. For Ni alloys, all the investigated elements exhibit negative interaction energies and hence the driving force of ISF segregation at 0 K. For Co alloys, elements from group-5 to group-9 show driving forces of segregation, except for Mn, Fe, and W. The interaction energy can be related to the lattice distortions, redistribution of charge density, and the density of states. The interaction energies are essential to thermodynamic models to determine stacking fault energies. The relationships between the energy and first-principles properties can be useful to determine materials property descriptors for machine learning or active learning models to guide the materials design using the stacking fault and local phase transformation strengthening in both FCC and γ' phases of Ni- and Co-based alloys.

1. Solutes generate different lattice distortions when placed in the ISF and the FCC planes. We found that interaction energies increase when the difference between the 1NN bond lengths in the ISF and the FCC regions increases. The interaction energies of 3d transition metal elements with lower lattice misfits are more likely to be controlled by electronic and magnetic interactions.

2. The charge density redistribution around the solute atoms shows that V, Cr, Ni, Mo, Ru, Rh, Re, and Ir are more likely to redistribute charge density to the 1NN bonding in the ISF relative to the FCC region, leading to negative interaction energies in Co. For the Ni system, the redistribution around the Ni atoms are stronger when the solutes are placed in the ISF plane compared to the FCC region, resulting in negative interaction energies for all the elements.

3. The bonding environment is governed by the d-d hybridization between the solutes and Co/Ni atoms. Pseudo-gap analysis reveals that the interaction energies of 3d elements are more likely to be controlled by the gap differences between ISF and FCC planes.

4. The d-d hybridization leads to changes in the local magnetizations around the solute plane of the supercell. The interaction energy generally becomes more negative when the magnetic difference decreases between the ISF and FCC regions after adding the solute atoms. 3d elements show only weak correlation with differences in the magnetic moment between the ISF and FCC regions. For Cr and Mn, Cr interacts with adjacent (111) planes of the supercell while Mn only interact with the solute plane, which may further leads to a change in the interaction energies in Co and Ni.

CRediT authorship contribution statement

Dongsheng Wen: Conceptualization, Methodology, Validation, Visualization, Data curation, Writing – original draft, Writing – review & editing. **Michael S. Titus:** Conceptualization, Methodology, Software, Resources, Writing – review & editing, Supervision, Project administration, Funding acquisition.

Declaration of competing interest

The authors declare that they have no known competing financial interests or personal relationships that could have appeared to influence the work reported in this paper.

Data availability

Data will be made available on request.

Acknowledgments

This material is based upon work supported by the National Science Foundation, USA under Grant No. (CAREER DMR-1848128). The authors would additionally like to acknowledge Purdue University, USA for supporting this work through start-up funds. This research was supported in part through computational resources provided by Information Technology at Purdue, West Lafayette, Indiana. The authors would like to thank Longsheng Feng and Prof. Yunzhi Wang in Ohio State University for thorough discussions on segregation isotherm.

Appendix A. Supplementary data

Supplementary material related to this article can be found online at https://doi.org/10.1016/j.commatsci.2023.112033.

References

[1] H. Suzuki, Chemical interaction of solute atoms with dislocations, Science reports of the Research Institutes, Tohoku University. Ser. A 4 (1952) 455–463.
[2] H. Suzuki, Segregation of solute atoms to stacking faults, Journal of the Physical Society of Japan 17 (2) (1962) 322–325.
[3] M.S. Titus, R.K. Rhein, P.B. Wells, P.C. Dodge, G.B. Viswanathan, M.J. Mills, A. Van der Ven, T.M. Pollock, Solute segregation and deviation from bulk thermodynamics at nanoscale crystalline defects, Science Advances 2 (12) (2016) e1601796.
[4] T. Hickel, S. Sandlöbes, R.K. Marceau, A. Dick, I. Bleskov, J. Neugebauer, D. Raabe, Impact of nanodiffusion on the stacking fault energy in high-strength steels, Acta Materialia 75 (2014) 147–155.
[5] C. Niu, C.R. LaRosa, J. Miao, M.J. Mills, M. Ghazisaeidi, Magnetically-driven phase transformation strengthening in high entropy alloys, Nature Communicatoin 9 (1) (2018) 1–9.
[6] M.S. Titus, A. Mottura, G.B. Viswanathan, A. Suzuki, M.J. Mills, T.M. Pollock, High resolution energy dispersive spectroscopy mapping of planar defects in L12-containing Co-base superalloys, Acta Materialia 89 (2015) 423–437.
[7] Y. Rao, T.M. Smith, M.J. Mills, M. Ghazisaeidi, Segregation of alloying elements to planar faults in γ'-Ni3Al, Acta Materialia 148 (2018) 173–184.
[8] T.M. Smith, B. Good, T.P. Gabb, B.D. Esser, A.J. Egan, L.J. Evans, D.W. McComb, M.J. Mills, Effect of stacking fault segregation and local phase transformations on creep strength in Ni-base superalloys, Acta Materialia 172 (2019) 55–65.
[9] L. Feng, Y. Rao, M. Ghazisaeidi, M.J. Mills, Y. Wang, Quantitative prediction of Suzuki segregation at stacking faults of the $\gamma\prime$phase in Ni-base superalloys, Acta Materialia 200 (2020) 223–235.
[10] D.T. Pierce, J.A. Jiménez, J. Bentley, D. Raabe, C. Oskay, J. Wittig, The influence of manganese content on the stacking fault and austenite/ε-martensite interfacial energies in Fe–Mn–(Al–Si) steels investigated by experiment and theory, Acta Materialia 68 (2014) 238–253.
[11] D.T. Pierce, J.A. Jiménez, J. Bentley, D. Raabe, J.E. Wittig, The influence of stacking fault energy on the microstructural and strain-hardening evolution of Fe–Mn–Al–Si steels during tensile deformation, Acta Materialia 100 (2015) 178–190.
[12] M.S. Titus, Y.M. Eggeler, A. Suzuki, T.M. Pollock, Creep-induced planar defects in L12-containing Co-and CoNi-base single-crystal superalloys, Acta Materialia 82 (2015) 530–539.
[13] S. Lu, S. Antonov, F. Xue, L. Li, Q. Feng, Segregation-assisted phase transformation and anti-phase boundary formation during creep of a γ'-strengthened Co-based superalloy at high temperatures, Acta Materialia 215 (2021) 117099.
[14] Y.M. Eggeler, J. Müller, M.S. Titus, A. Suzuki, T.M. Pollock, E. Spiecker, Planar defect formation in the γ' phase during high temperature creep in single crystal CoNi-base superalloys, Acta Materialia 113 (2016) 335–349.
[15] G.B. Viswanathan, R. Shi, A. Genc, V.A. Vorontsov, L. Kovarik, C.M.F. Rae, M.J. Mills, Segregation at stacking faults within the γ' phase of two Ni-base superalloys following intermediate temperature creep, Scripta Materialia 94 (2015) 5–8.
[16] T.M. Smith, B.D. Esser, N. Antolin, G.B. Viswanathan, T. Hanlon, A. Wessman, D. Mourer, W. Windl, D.W. McComb, M.J. Mills, Segregation and η phase formation along stacking faults during creep at intermediate temperatures in a Ni-based superalloy, Acta Materialia 100 (2015) 19–31.
[17] D. Wen, M.S. Titus, First-principles study of suzuki segregation at stacking faults in disordered face-centered cubic Co-Ni alloys, Acta Materialia 221 (2021) 117358.
[18] R.C. Reed, The Superalloys: Fundamentals and Applications, Cambridge University Press, 2008.
[19] G. Han, I. Jones, R. Smallman, Direct evidence for suzuki segregation and cottrell pinning in MP159 superalloy obtained by FEG (S) TEM/EDX, Acta Materialia 51 (10) (2003) 2731–2742.

[20] L. Feng, S.B. Kannan, A. Egan, T. Smith, M.J. Mills, M. Ghazisaeidi, Y. Wang, Localized phase transformation at stacking faults and mechanism-based alloy design, Acta Materialia 240 (2022) 118287.
[21] G.B. Olson, M. Cohen, A general mechanism of martensitic nucleation: Part I. General concepts and the FCC-HCP transformation, Metall. Trans. A 7 (12) (1976) 1897–1904.
[22] N. Ma, S. Dregia, Y. Wang, Solute segregation transition and drag force on grain boundaries, Acta Materialia 51 (13) (2003) 3687–3700, http://dx.doi.org/10.1016/S1359-6454(03)00184-8, URL https://linkinghub.elsevier.com/retrieve/pii/S1359645403001848.
[23] X.L. Liu, G. Lindwall, T. Gheno, Z.-K. Liu, Thermodynamic modeling of Al–Co–Cr, Al–Co–Ni, Co–Cr–Ni ternary systems towards a description for Al–Co–Cr–Ni, CALPHAD 52 (2016) 125–142.
[24] R. Li, S. Lu, D. Kim, S. Schönecker, J. Zhao, S.K. Kwon, L. Vitos, Stacking fault energy of face-centered cubic metals: thermodynamic and ab initio approaches, Journal of Physics: Condensed Matter 28 (39) (2016) 395001.
[25] G. Kresse, J. Furthmüller, Efficient iterative schemes for ab initio total-energy calculations using a plane-wave basis set, Physical Review B 54 (16) (1996) 11169.
[26] G. Kresse, D. Joubert, From ultrasoft pseudopotentials to the projector augmented-wave method, Physical Review B 59 (3) (1999) 1758.
[27] P.E. Blöchl, Projector augmented-wave method, Physical Review B 50 (24) (1994) 17953.
[28] J.P. Perdew, K. Burke, M. Ernzerhof, Generalized gradient approximation made simple, Physical Review Letters 77 (18) (1996) 3865.
[29] M. Methfessel, A. Paxton, High-precision sampling for brillouin-zone integration in metals, Physical Review B 40 (6) (1989) 3616.
[30] P.E. Blöchl, O. Jepsen, O.K. Andersen, Improved tetrahedron method for brillouin-zone integrations, Physical Review B 49 (23) (1994) 16223.
[31] S. Ogata, J. Li, S. Yip, Ideal pure shear strength of aluminum and copper, Science 298 (5594) (2002) 807–811.
[32] W. Wang, S. Shang, Y. Wang, K. Darling, S. Mathaudhu, X. Hui, Z. Liu, Electron localization morphology of the stacking faults in Mg: a first-principles study, Chemical Physics Letters 551 (2012) 121–125.
[33] M. Wolloch, G. Levita, P. Restuccia, M. Righi, Interfacial charge density and its connection to adhesion and frictional forces, Physical Review Letters 121 (2) (2018) 026804.
[34] R.E. Cohen, Origin of ferroelectricity in perovskite oxides, Nature 358 (6382) (1992) 136–138.
[35] L. Delehouzee, A. Deruyttere, The stacking fault density in solid solutions based on copper, silver, nickel, aluminium and lead, Acta Metallurgica 15 (5) (1967) 727–734.
[36] P. Gallagher, The influence of alloying, temperature, and related effects on the stacking fault energy, Metallurgical Transactions 1 (9) (1970) 2429–2461.
[37] H. Song, F. Tian, Q.-M. Hu, L. Vitos, Y. Wang, J. Shen, N. Chen, Local lattice distortion in high-entropy alloys, Physical Review Materials 1 (2) (2017) 023404.
[38] D.A. Papaconstantopoulos, et al., Handbook of the Band Structure of Elemental Solids, Springer, 1986.
[39] J.-H. Xu, T. Oguchi, A. Freeman, Crystal structure, phase stability, and magnetism in Ni3V, Physical Review B 35 (13) (1987) 6940.
[40] Q. Hu, R. Yang, D. Xu, Y. Hao, D. Li, W. Wu, Geometric and electronic structure of Ti2AlX (X=V, Nb, or Ta), Physical Review B 68 (5) (2003) 054102.
[41] Q.-M. Hu, L. Vitos, R. Yang, Theoretical investigation of the ω-related phases in TiAl-Nb/Mo alloys, Physical Review B 90 (5) (2014) 054109.